Chemical Science

ROYAL SOCIETY OF CHEMISTRY

EDGE ARTICLE

View Article Online
View Journal | View Issue

Cite this: *Chem. Sci.*, 2023, **14**, 8408

All publication charges for this article have been paid for by the Royal Society of Chemistry

The H-NOX protein structure adapts to different mechanisms in sensors interacting with nitric oxide†

Byung-Kuk Yoo,‡[a] Sergei G. Kruglik,[b] Jean-Christophe Lambry,[a] Isabelle Lamarre,[a] C. S. Raman,[c] Pierre Nioche[de] and Michel Negrerie *[a]

Received 31st March 2023
Accepted 5th July 2023

DOI: 10.1039/d3sc01685d

rsc.li/chemical-science

Some classes of bacteria within phyla possess protein sensors identified as homologous to the heme domain of soluble guanylate cyclase, the mammalian NO-receptor. Named H-NOX domain (Heme-Nitric Oxide or OXygen-binding), their heme binds nitric oxide (NO) and O_2 for some of them. The signaling pathways where these proteins act as NO or O_2 sensors appear various and are fully established for only some species. Here, we investigated the reactivity of H-NOX from bacterial species toward NO with a mechanistic point of view using time-resolved spectroscopy. The present data show that H-NOXs modulate the dynamics of NO as a function of temperature, but in different ranges, changing its affinity by changing the probability of NO rebinding after dissociation in the picosecond time scale. This fundamental mechanism provides a means to adapt the heme structural response to the environment. In one particular H-NOX sensor the heme distortion induced by NO binding is relaxed in an ultrafast manner (~15 ps) after NO dissociation, contrarily to other H-NOX proteins, providing another sensing mechanism through the H-NOX domain. Overall, our study links molecular dynamics with functional mechanism and adaptation.

Introduction

To adapt to environmental conditions, diverse bacteria have developed heme-based protein sensors[1] to monitor changes of dioxygen (O_2) and nitric oxide (NO) concentrations in order to trigger avoidance reactions or changes in their metabolism. The sensing function is ensured by the b-type heme which coordinates diatomics and transduces the binding information to another protein domain.[2] In mammals, soluble guanylate cyclase (sGC) is the endogenous heme-based NO receptor expressed in the cytoplasm of many cells and converts GTP to the second messenger cGMP.[3] In particular bacteria species, heme sensors have been identified[4–6] by sequence homology with the β1-subunit heme domain of sGC (ESI, Fig. S1†), suggesting a bacterial origin for eukaryotic sGC.[5–7] This domain was named H-NOX for Heme-Nitric Oxide or OXygen-binding since it may bind either NO[8] or O_2 (ref. 9 and 10) (but also CO[11]). Whereas the H-NOX domain of mammalian sGC is coupled to a cGMP-synthase, the bacterial ones are associated either with histidine kinase, diguanylate cyclase or methyl-accepting chemotaxis catalytic domains.[12]

Since their discovery, bacterial H-NOXs from three species were particularly investigated.[5,6,8,13–17] The anaerobe *Caldanaerobacter subterraneus tengcongensis* (*Ct*, formerly named *Thermoanaerobacter tengcongensis*)[18,19] lives optimally at high temperature (75–86 °C)[18] whereas the aquatic photosynthetic bacterium *Nostoc punctiforme* (*Np*) lives on moist rock and soil along the bottom of freshwater[20] and grows preferentially in the temperature range 15–40 °C. The mesophile and strict anaerobe *Clostridium botulinum* (*Cb*) which possesses also a H-NOX domain is toxic for mammals. The physiological function of all bacterial H-NOXs is not firmly established but emerges for some species. A sub-family of H-NOX sensors found in facultative anaerobes do not form a stable complex with O_2, similarly with mammalian sGC, and are considered as specific NO-sensors involved in the regulation of biofilm formation and/or quorum sensing signaling.[21,22] They include the metal reducing *Shewanella oneidensis*, whose H-NOX sensor regulates a kinase,[23] two *Vibrio* species[24,25] and the marine species

[a]*Laboratoire d'Optique et Biosciences, INSERM U-1182, Ecole Polytechnique, 91120 Palaiseau, France. E-mail: michel.negrerie@polytechnique.edu*

[b]*Laboratoire Jean Perrin, Institut de Biologie Paris-Seine, Sorbonne Université, CNRS, 75005 Paris, France*

[c]*Department of Pharmaceutical Sciences, School of Pharmacy, University of Maryland, Baltimore, Maryland 21201, USA*

[d]*Environmental Toxicity, Therapeutic Targets, Cellular Signaling and Biomarkers, UMR S1124, Centre Universitaire des Saints-Pères, Université Paris Descartes, 75006 Paris, France*

[e]*Structural and Molecular Analysis Platform, BioMedTech Facilities, INSERM US36-CNRS-UMS2009, Paris Université, Paris, France*

† Electronic supplementary information (ESI) available. See DOI: https://doi.org/10.1039/d3sc01685d

‡ Present address: Thermo Fisher Scientific, Kenilworth, New Jersey, USA.

Shewanella woodyi whose H-NOX regulates a diguanylate cyclase or phosphodiesterase.[26,27]

Sometimes considered as "models" for sGC activation,[17,28] bacterial H-NOXs are involved in various signaling pathways. Does the same activation mechanism take place in all H-NOXs? In sGC, the binding of NO to the heme induces the bond cleavage between the proximal histidine and heme iron, leading to a five-coordinate Fe^{2+} with NO (5c-NO) which triggers a structural change in the H-NOX domain (Fig. 1) which propagates through the interface between subunits.[29] The bacterial H-NOX sensors from the *Cb*, *Np* and *Ct* species disclose functional differences with sGC and depart from each other. *Np* H-NOX possesses properties of either a NO-sensor or a regulator of redox potential[30] whereas *Cb* H-NOX can bind the sGC stimulator BAY-412272.[31] *Ct* H-NOX binds O_2 with high affinity whereas *Np* H-NOX does not bind O_2 but becomes oxidized.[30,32] The large affinity of NO for *Cb* H-NOX[32] suggests a function related to NO toxicity. Considering the large range of environments to which bacteria have adapted, one may infer that the dynamical properties of a particular H-NOX can not be merely transposed to others, as exemplified by truncated sGC constructs.[33,34]

Here, we report on the heme structural dynamics of the H-NOX sensors from *Cb*, *Np* and *Ct* bacteria species reacting with NO in light of their possible role as NO-sensors compared with mammalian sGC. Using time-resolved electronic absorption spectroscopy in the pico- to nanosecond time range, we probed and quantified the non-equilibrium heme relaxation and dynamics induced by NO dissociation. Since these bacteria live in different temperature ranges, we investigated their dynamics as a function of temperature. Especially, nitrosylated H-NOXs can exist as a mixture of 5c-NO and 6c-(His)-NO liganded species, depending on the temperature, whose proportion influences their sensing properties in contrast with mammalian sGC which is always 5c-NO. Our results show that the various H-NOXs control differently the dynamics of NO as a function of temperature and adapt their heme structural response. Only in *Ct* H-NOX the heme distortion, which relaxes in an ultrafast manner after NO dissociation, intervenes in the sensing mechanism.

Results and discussion

Heme coordination dependence on temperature

The absorption spectra of unliganded reduced H-NOXs exhibit a Soret band at 431–433 nm (Fig. 2) similarly with sGC.[35] After the addition of NO at 20 °C this band shifts differently for the three proteins: to 420 nm (with a very small shoulder at 399 nm) for *Ct*, 416 nm (larger shoulder at 399 nm) for *Np* and 409 nm for *Cb*, contrastingly to nitrosylated sGC whose Soret maximum is positioned at 399 nm.[35] These different positions result from the varying equilibrium between 6c-(His)-NO and 5c-NO heme as a function of temperature, whereas mammalian sGC was never observed in 6c-(His)-NO steady-state even at 4 °C and forms a unique 5c-NO species.[36,37] With a large proportion of 5c-NO heme at 20 °C, the *Cb* H-NOX sensor appears the closest to mammalian sGC. Whereas *Cb* and *Np* sensors precipitated and oxidized at $T > 55$ °C, *Ct* H-NOX could be heated up to 76 °C where it was mainly in the 5c-NO state. Consequently, we investigated the heme dynamics of H-NOXs as a function of temperature.

We measured time-resolved absorption by photodissociating bound NO (excitation 50 fs pulse at 564 nm) and measuring successive transient spectra (50 fs pulse at 375–500 nm) in the picosecond time range (see detailed Experimental methods in ESI†). The absolute transient spectra $S(t)$ were recorded at each time delay but the difference spectra $S(t)$–S_0 are presented to make apparent the spectral changes (S_0 is the spectrum before photodissociation of NO).

NO and heme picosecond dynamics in *Clostridium botulinum* H-NOX

The heme dynamics of *Cb* H-NOX was probed at three temperatures (4, 20 and 40 °C) where it is stable. NO dissociation leads to complex changes in the spectra depending upon the temperature (Fig. 3 and ESI, Fig. S3†). At 4 °C the maximum of induced absorption (positive band) is centered at 434 nm but the bleaching (negative band) is composed of two minima at 401 and 416 nm which indicate two photo-induced species, assigned to the disappearance of 5c-NO species, forming a 4c

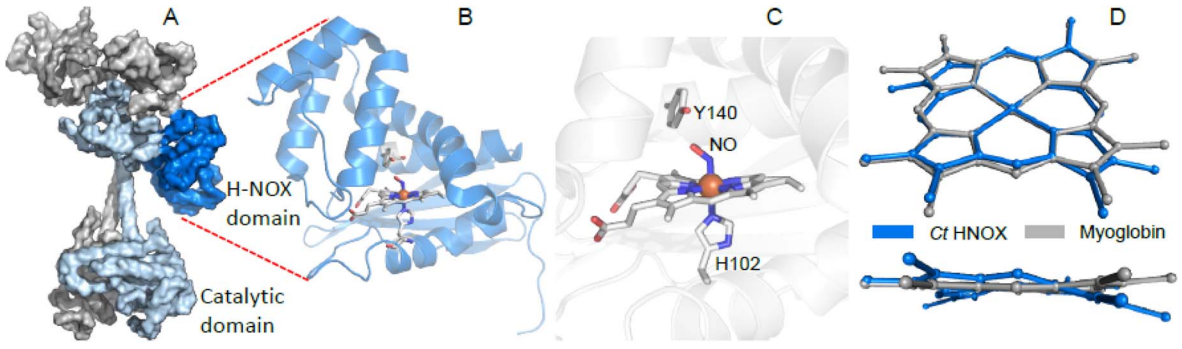

Fig. 1 The H-NOX domain. (A) Overall shape of the human dimeric soluble guanylate cyclase in its activated state (PDB file 7D9S). Grey represents the α1 subunit, blue the β1 subunit and dark blue the H-NOX domain. (B) Tertiary structure of the homologous H-NOX protein from the bacteria *Caldanaerobacter tengcongensis* (PDB file 5JRV). (C) Close-up of the NO-bound distorted heme of *Ct* H-NOX. (D) Distortion of the NO-bound heme of *Ct* H-NOX (blue) is compared with the nitrosylated heme of myoglobin (PDB file 2FRK).

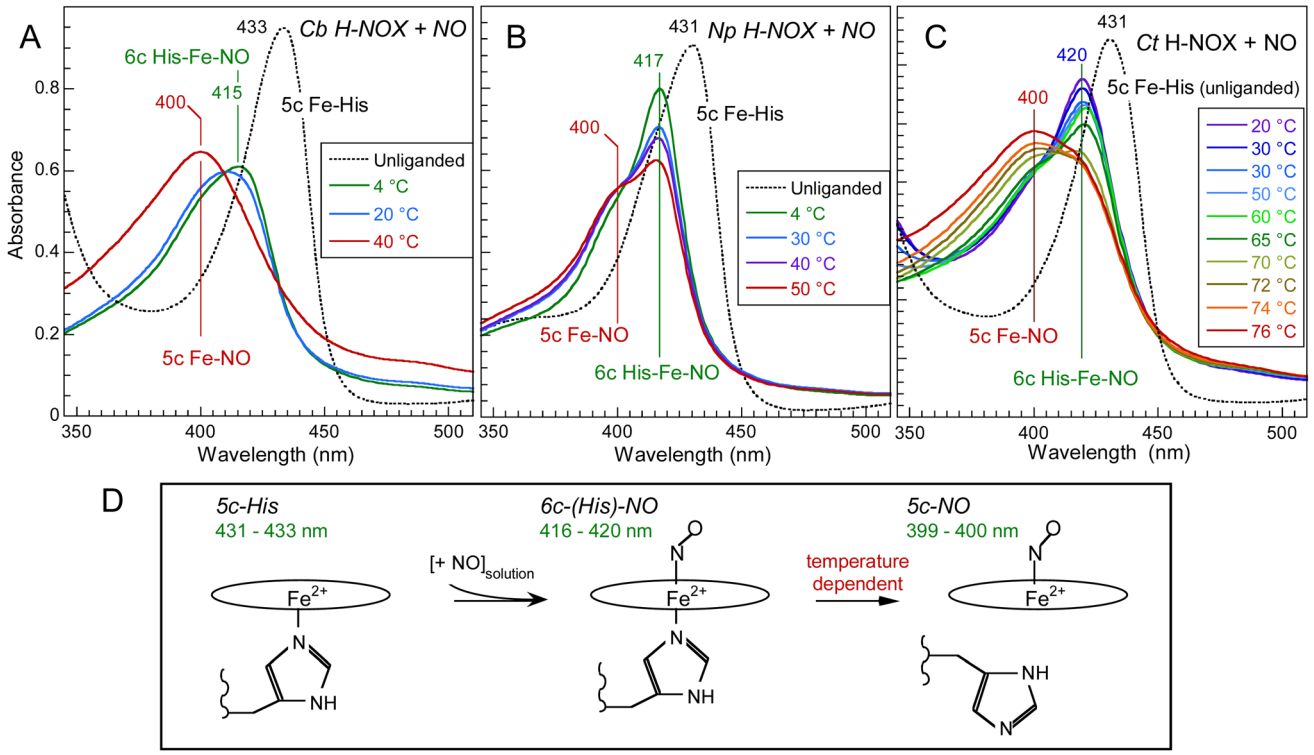

Fig. 2 Temperature dependence of the electronic absorption spectra of NO-liganded *Cb* H-NOX (A), *Np* H-NOX (B) and *Ct* H-NOX (C). [NO] = 200 μM. Note the difference in the temperature ranges. The spectra of all unliganded species were recorded at 20 °C. The Q-bands are displayed in ESI, Fig. S2.† (D) Heme coordination states involved with corresponding Soret band wavelength.

heme similarly to sGC,[35] and of 6c-(His)-NO, forming a 5c-His heme similarly to myoglobin.[38] As the temperature increases up to 40 °C the 6c-(His)-NO contribution at 416 nm disappeared from the bleaching (Fig. 3A, D and S3A† for 20 °C).

The data matrix comprises 60 spectra as a function of time and was analyzed by Singular Value Decomposition (SVD; see ESI Experimental methods†) in order to identify processes (spectral components) and their evolution (kinetic components). Only two significative components appeared in the first step of SVD calculation and they already represent the spectra of two readily identified processes (Fig. 3). In a second step we calculated the spectra associated with individual species, as shown in the ESI Appendix 1.† The two SVD spectral components (Fig. 3B, E and S3B†) have very different singular values (SV1 > 10 × SV2): the first one corresponds to NO dissociation and its kinetics describes NO rebinding (Fig. 3C, F and ESI, Fig. S3C†). Comparison of the SVD1 spectra at three temperatures (ESI, Fig. S4†) directly shows the change of heme coordination after NO dissociation. The spectrum of 4c heme is broad[35] and largely overlaps that of 5c-His, so that the SVD1 component contains both 5c-NO and 6c-His-NO contributions. Accordingly, two time constants are revealed in the fitted SVD1 kinetics (Table 1), respectively $\tau_5 = 6.9 \pm 0.2$ ps for 4c + NO → 5c-NO and $\tau_6 = 23 \pm 2$ ps for 5c-His + NO → 6c-(His)-NO. The amplitude of the first one increases from $A_5 = 81$ to 91% of the total geminate rebinding process at 4 and 40 °C, respectively (Table 1).

A very fast component is also present in SVD1 kinetics due to excited state relaxation with time constant $\tau_{ex} = 1.5 \pm 0.2$ ps (ESI Table S1†). Interestingly, a recent study has identified by transient X-ray absorption a similar fast relaxation (0.9 ps) in myoglobin attributed to heme core expansion and completion of the iron out-of plane displacement after photodissociation of CO,[39] a process which could be universal to b-type hemes.

The second spectral component SVD2 (Fig. 3E), markedly different from SVD1, describes a shift of the Soret band from ~425 nm to 433 nm and is associated with a kinetic component (ESI, Fig. S5†) whose time constant ($\tau_3 = 35 \pm 4$ ps) does not vary with temperature. In SVD2 spectrum the bleaching does not correspond to NO dissociation but to the decrease of the 4c Soret band at ~425 nm with an increase at 433 nm. Consequently, SVD2 describes the heme transition 4c → 5c-His, *i.e.* the proximal His rebinding which occurs whatever the temperature. The comparison of SVD2 spectrum with the raw transient spectra at +50 ps and that at +4 ps (ESI, Fig. S6A†) confirms this assignment. The dissociated 4c heme mainly interacts with NO (SVD1 process) and only a small proportion of 4c heme reassociates with proximal His and produces a low-amplitude SVD2 component. This process was similarly measured in cytochrome c′[40] and in sGC.[41]

To show the difference of induced absorption at 4 °C and 40 °C (Fig. 3A and D) we calculated the absolute spectrum of the photoproduct at Δt = +4 ps (ESI, Fig. S6B†): it is blue shifted at high temperature when the transient 4c heme is ~100%, but is a mixture 4c/5c-His at 4 °C. The NO rebinding time constant (6.9 ± 0.5 ps) and the geminate yield (~99%) for *Cb* H-NOX are similar to those measured for sGC.[41] The predominance of 5c-

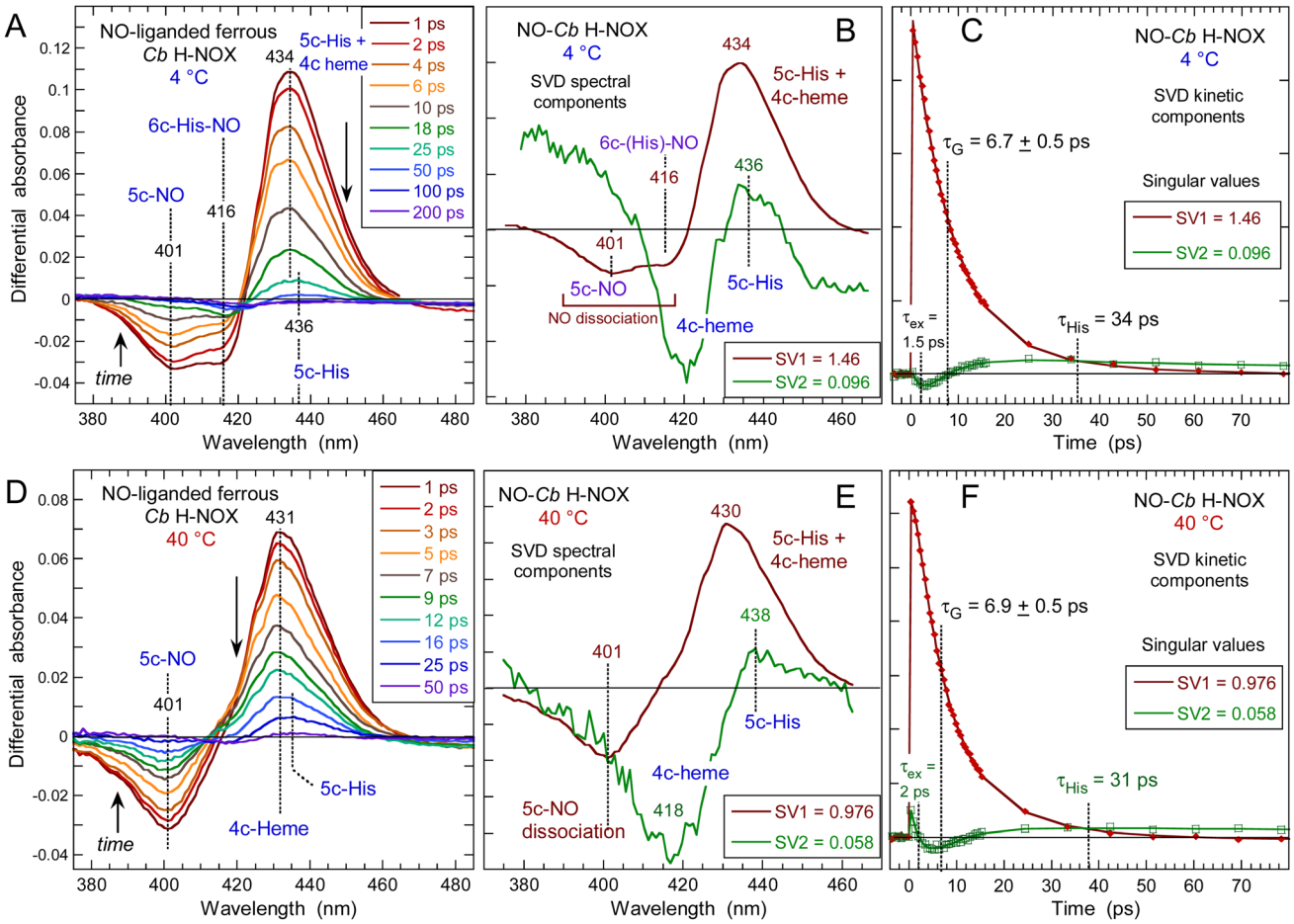

Fig. 3 Time-resolved absorption data for NO interacting with *Cb* H-NOX at $T = 4$ °C and 40 °C. The data at 20 °C can be seen in ESI, Fig. S3.† (A and D) Transient spectra at selected time delays after photodissociation of NO. (B and E) Spectral components from SVD analysis of the time-wavelength matrix. (C and F) SVD kinetic components describing the evolution of spectral components with fitted parameters in ESI Table S1.†

NO in *Cb* H-NOX whatever the temperature is due to a small energy barrier for Fe^{2+}–His bond cleavage, which explains that binding of the stimulator BAY-412272 to *Cb* H-NOX can change its conformation, similarly with sGC.[31] Linked to this property is the observation that two single sGC mutants are only activated in the simultaneous presence of NO and the stimulator riociguat, but not NO alone.[42] For these sGC mutants the energy threshold for activation by NO alone is increased, but the stimulator decreases this energy and facilitates the cleavage of the Fe–His bond by NO.

NO and heme dynamics in *Nostoc punctiforme* H-NOX

The *Np* H-NOX discloses similar dynamics as *Cb* but in a different temperature range (Fig. 4 and ESI, Fig. S7†). At 4 °C, the evolution of transient spectra (ESI, Fig. S7A†) shows an

Table 1 Time constants and relative amplitudes of NO geminate rebinding for the three H-NOXs. The constant term corresponds to a much longer component assigned to bimolecular rebinding

			6c-(His)-NO		
H-NOX	T	5c-NO, τ_5 (A_5)	τ_6 (A_6)	τ'_6(A'_6)	Constant (A_C)
Cb	4 °C	6.7 ps (*0.81*)	23 ps (*0.19*)	—	(*<1*)
	20 °C	7.1 ps (*0.87*)	24 ps (*0.13*)	—	(*<1*)
	40 °C	6.9 ps (*0.91*)	23 ps (*0.09*)	—	(*<1*)
Np	4 °C	5.6 ps (*0.38*)	32 ps (*0.20*)	290 ps (*0.32*)	(*0.10*)
	20 °C	5.0 ps (*0.44*)	38 ps (*0.17*)	309 ps (*0.29*)	(*0.10*)
	50 °C	5.8 ps (*0.61*)	36 ps (*0.11*)	305 ps (*0.17*)	(*0.11*)
Ct	20 °C	—	7.3 ps (*0.78*)	—	(*0.22*)
	74 °C	7.0 ps (*0.81*)	—	—	(*0.19*)

extremely small shift of the isosbestic point (423 nm) indicating that one process largely predominates. The data matrix was analysed by SVD (ESI, Table S2 and Appendix 1†) and the kinetics was fitted to the sum of three exponential terms (Table 1). At 4 °C, the main SVD spectral component (ESI, Fig. S7B†) corresponds to NO geminate rebinding to the 5c-His heme (from 6c-(His)-NO dissociation) which proceeds with two time constants: $\tau_6 = 32$ ps and $\tau_6' = 290$ ps. The first one is due to NO located within the heme pocket and the second one is due to NO having left the heme pocket but still within the protein core (290 ps is too fast for diffusion from the solution). The contribution of 5c-NO dissociation is very small and is contained in the SVD2 component together with an even smaller contribution of 5c-His reformation from 4c heme ($\tau_{His} = 99$ ps) as in sGC.[41] At 50 °C the large shift of the isosbestic point (420 to 426 nm) in transient spectra (ESI, Fig. S7G†) indicates two processes. Thus, as the temperature raises, the relative amplitudes of NO rebinding and of proximal His rebinding, both to the 4c heme, increase while that of 6c-(His)-NO decreases (Fig. 4B and Table 1) with similar time constants. Of note, NO rebinding to the 4c heme occurs much faster ($\tau_5 = 5.8 \pm 0.5$ ps) than that of proximal His ($\tau_{His} = 118 \pm 19$ ps).

The time constant of NO rebinding to the 4c heme is similar for *Np*, *Cb* H-NOX (7 ± 0.5 ps) and sGC (7.5 ps)[41] but with a smaller yield (87% *versus* 99 and 96%) which indicates a lower energy barrier for NO exiting the heme pocket. *Np* H-NOX is never fully 6c-(His)-NO nor 5c-NO whatever the temperature (Fig. 2 and 4B) and it binds much less the sGC stimulator BAY-412272 than does *Cb*.[31] Its properties depart from those of sGC and *Cb* H-NOX. In all H-NOXs the proximal His recombines rapidly with the 4c heme (35–130 ps), and NO which diffuses from the solution in the μs time range always binds to a 5c-His heme. Consequently, the changing proportion of 5c-NO/6c-(His)-NO as a function of temperature influences only the NO k_{off} rate, but not the k_{on} rate which involves NO from the solution.

NO and heme dynamics in *Caldanaerobacter subterraneus tengcongensis* H-NOX

Following NO dissociation from *Ct* H-NOX the transient spectra (Fig. 5) disclose more complex features than observed for the other sensors. At 20 °C *Ct* H-NOX is essentially 6c-(His)-NO and the minimum of bleaching at 421 nm rapidly decreases due to NO recombination to the 5c-His dissociated heme (Fig. 5A). The maximum of induced absorption centered at 442 nm did not shift during the first 6 ps but rapidly vanishes after 12 ps. The large shift of the isosbestic point from 431 to 443 nm indicates that another process takes place, at the origin of the second bleaching centered at 429 nm which develops from ~8 ps to ~100 ps, then stays constant.

Ct is a strict anaerobe having a physiological temperature growth >70 °C in native conditions and we thus probed the heme-NO dynamics at 74 °C. Dissociation of NO generates the broad bleaching centered at 400 nm (Fig. 5D) indicating that the 5c-NO heme species is largely dominant with the minor presence of 6c-(His)-NO at 421 nm. The bleaching at 429 nm due to the second process is more pronounced than at 20 °C so that the induced absorption of transient 4c heme (425–428 nm) is not discernible.

The individual spectral components of the two processes were identified by global SVD analysis (Fig. 5B, E and ESI Appendix 1†) with their associated kinetics (Fig. 5C and F) which were fitted to the sum of two exponential decays and a constant term (Table 1). We first describe the SVD2 spectrum (smaller singular value) which represents the rebinding of NO (Fig. 5C and F). The bleaching part of SVD2 represents the initial 6c-(His)-NO (420 nm) at 20 °C and 5c-NO heme (400 nm) at 74 °C whereas the induced absorption (443–445 nm) is due to the 5c-His dissociated heme at 20 °C but mainly to the 4c heme at 74 °C.

Remarkably NO recombines with a unique time constant $\tau = 7$ ps at both temperatures without slower decays as measured for *Cb*, *Np* (Table 1) or other proteins.[38] The fact that

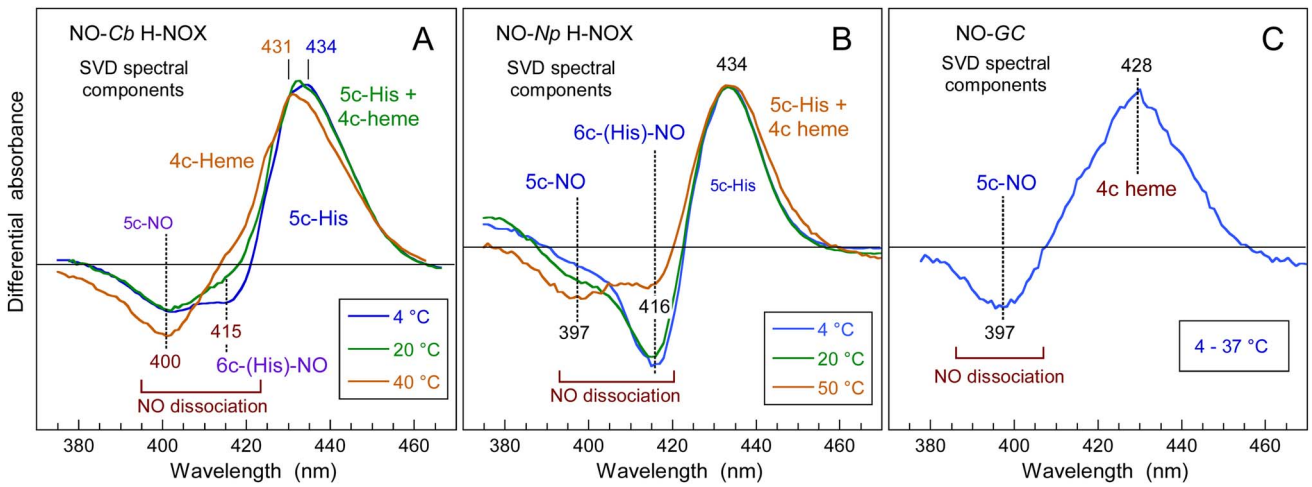

Fig. 4 Spectral components of NO geminate rebinding obtained from SVD analysis of the matrix of transient spectra for *Cb* H-NOX (A) and *Np* (B) H-NOX sensors at different temperatures compared to bovine (*Bos taurus*) soluble guanylate cyclase (C) whose transient spectrum does not change as *T* is raised. Analysis of the full data set for *Np* is shown in ESI, Fig. S7 and Table S2.†

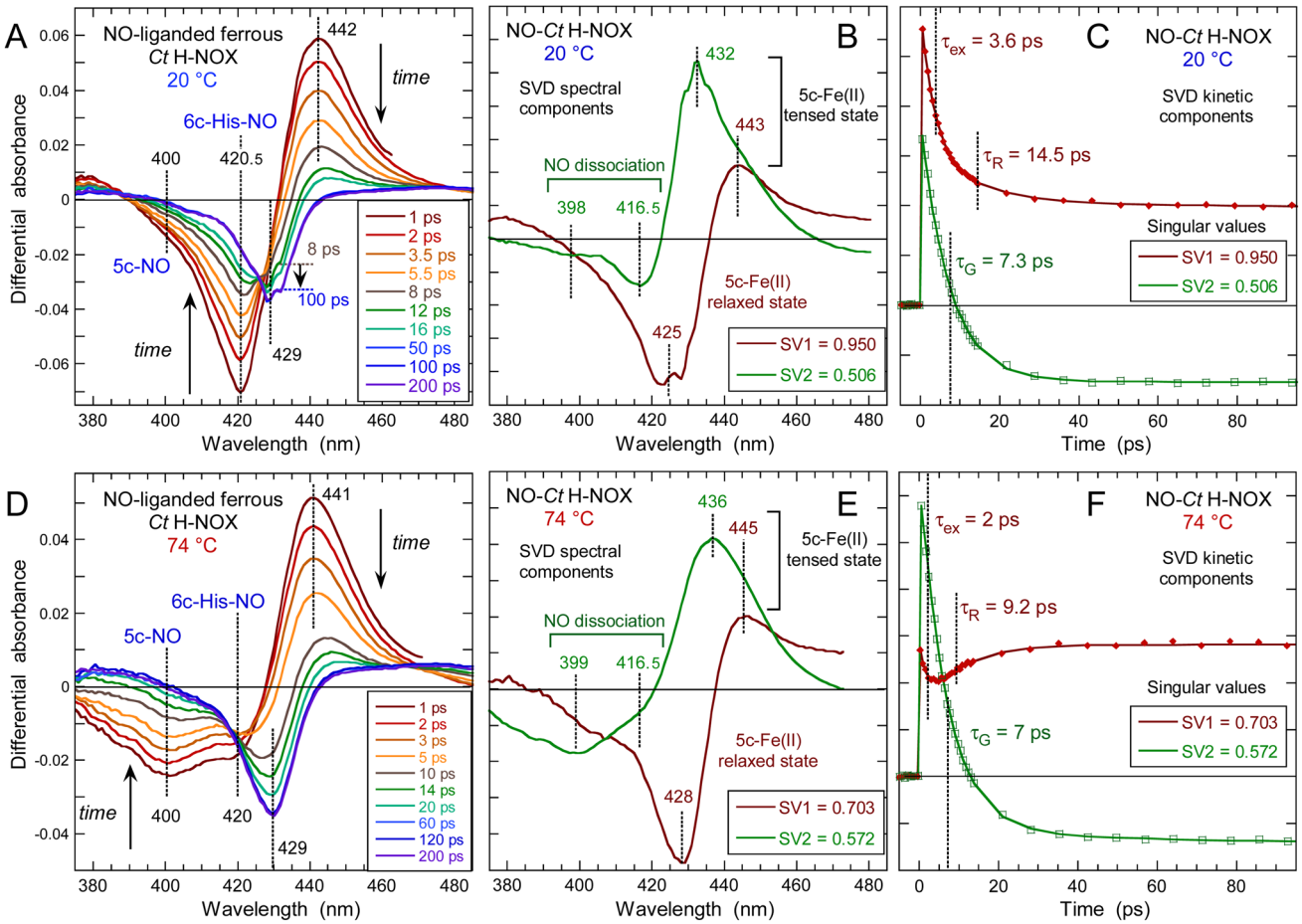

Fig. 5 Time-resolved absorption data for NO interacting with *Ct* H-NOX at two different temperatures. (A and D) Transient spectra at selected time delays after NO photodissociation at 20 °C and 74 °C, respectively. (B and E) Spectral components from SVD analysis of the time-wavelength matrices data. (C and F) Associated kinetic components from SVD analysis. Parameters of the SVD kinetics fit in Table S3.†

NO rebinds here to the 5c-His heme as fast as to the 4c heme is evidenced by the superposition of transient spectra at +1 and +3 ps (ESI, Fig. S8†) which demonstrates the same time evolution at both characteristic wavelengths (400 and 421 nm), supporting the unique value $\tau = 7.1 \pm 1$ ps for 5c-NO and 6c-(His)-NO. This result, observed only in *Ct* H-NOX, implies that the energy barrier for NO rebinding is as low in the 5c-His state as in the 4c state, most probably because the heme distortion induces a favorable configuration in the 5c-His state, as verified by dynamic simulations and Raman spectroscopy (see below).

Interactions of NO with side-chains of the heme pocket influence the on and off binding rates. We performed a dynamic simulation to probe NO trajectories in the 5c-His heme pocket (ESI, Fig. S9†). When NO is bound to the Fe^{2+} atom, its oxygen atom steadily stays at 3 Å from the hydroxyl of Tyr140, forming a stable hydrogen bond. NO can experience different trajectories: after dissociation, it may either remain in the heme pocket, leave it ($t > 500$ ps), or move back at 3.5 Å to heme Fe^{2+} where the oxygen atom of NO may reform a hydrogen bond (trajectory 3 in Fig. S9†). This position, favorable for Fe^{2+}–NO bond reformation, could provide a rationale for the low k_{off} rate. However, *Cb* H-NOX, which has a Tyr140 residue in the homologous position (ESI, Fig. S1†) has neither the same NO rebinding behavior nor the same k_{off} rate as *Ct* H-NOX (ESI, Table S4†). Consequently the influence of Tyr140 is not preponderant. The protein structure and heme distortion strongly influence the kinetics as shown by analysis of the SVD1 component.

The SVD1 spectrum (Fig. 5B and E) is similar at both temperatures and does not correspond to NO dissociation. The small induced absorption at 443–445 nm is assigned to the ferrous 5c-His heme whereas the pronounced deep bleaching at 425–428 nm indicates a decrease of the 5c-His heme absorption once formed. We first verified whether this decrease could be due to photo-oxidation by recording the transient absorption of ferric (Fe^{3+}) 6c-(His)-NO *Ct* H-NOX (ESI, Fig. S10†). The dissociated 5c-His ferric heme shows a characteristic broad induced absorption band centered at 390 nm which is clearly absent at any time delay from the transient spectra of the ferrous species (ESI, Fig. S10B†) so that photo-oxidation must be discarded. The SVD1 component thus describes a shift of the Soret band of the 5c-His ferrous heme without change of its redox or coordination states. Since only a deep bleaching is present at +200 ps without absorption band (Fig. 5A and D), the 5c-His heme spectrum has shifted and its absorption coefficient decreased. Thus, the SVD1

component represents the fast relaxation after NO dissociation of the non-equilibrium distorted heme toward a more stable state, similarly with O_2-bound *Ct* H-NOX.[43] Measurement at longer delay shows that spectra at +100 ps and +5 ns are identical (ESI, Fig. S11†) and that the bleaching persists, with an extremely slow relaxation whose time constant can only be estimated here as >5 ns, possibly in the μs time range.

Ultrafast *Ct* H-NOX heme relaxation upon electronic excitation in the absence of NO

To probe possible heme relaxation independently from NO, we measured the transient spectra of the 5c-His ferrous *Ct* H-NOX in pure argon (Fig. 6). The characteristic induced absorption band of the ferric species (ESI, Fig. S10†) is again absent and no photo-oxidation occurred. A deep bleaching is immediately formed at 428 nm and persists at longer time (>200 ps), exactly as in the case of NO dissociation, despite the absence of diatomic ligand. The shift of the isosbestic point (Fig. S12†) is due to two successive processes whose individual spectrum were identified by SVD analysis (ESI, Fig. S13†). The ground state depletion leads to the immediate formation of an electronic excited heme (450 nm) which fastly decays ($\tau_{ex1} = 1.2 \pm 0.2$ ps) to another excited species, itself relaxing ($\tau_{ex2} = 5.2 \pm 0.8$ ps) to a species responsible for the bleaching at 428 nm (Fig. 6B). This process agrees with the photophysics of heme proteins,[44] except that for *Ct* H-NOX the species +200 ps is not the same as in the ground state, but a structurally changed ferrous 5c-His heme. This rationale is supported by the fact that electronic excitation of distorted porphyrins induces conformational changes[45] and that in unliganded *Ct* H-NOX no possible ligand rebinding can occur. Remarkably, the difference spectrum at long time delays (>100 ps) is the same either measured in unliganded or NO-liganded *Ct* H-NOX (ESI, Fig. S14†), indicating the same species. Thus, a perturbation of the heme electronic orbitals, either directly or by diatomic detachment, induces a relaxation of the distorted heme of *Ct* contrarily to other H-NOXs and sGC. This relaxed heme will slowly evolve toward the 5c-His ground state on longer time scale.

We calculated the spectrum of this species from the transient spectrum at +200 ps (see Experimental methods in ESI†) which is red shifted with respect to the unliganded resting state (Fig. 6C). This red shift has same direction as that obtained for a *Ct* mutant (P115A) whose heme is relaxed compared to *Ct* wild type.[46] The spectral shift due to heme ruffling and its relaxation has been theoretically explained by the involvement of d orbitals energy level.[47]

Comparison of *Np* and *Ct* H-NOXs by steady-state Raman spectroscopy

We first describe the similar evolutions in the Raman spectra of both *Ct* and *Np* H-NOXs (Fig. 7) induced by the binding of NO. The most obvious is the disappearance of ν(Fe–His) mode and the up-shift of the ν_4 mode (from 1354/1357 cm^{-1} to 1372/1374 cm^{-1}). All modes and assignments are detailed in ESI, Table S5.† The ν(Fe–NO) stretching appears at 551/553 cm^{-1} and confirms the 6c-(His)-NO state of the heme[48] in both sensors at 20 °C because this mode has always a lower frequency for 5c hemes (525 cm^{-1} for sGC).[13,49] The frequency of the mode ν_3 at 1470/1472 cm^{-1} indicates a 5c-His high spin heme for both proteins in the ferrous unliganded state (Fig. 7a and c). Upon NO binding ν_3 shifts to a complex band (1501–1505 cm^{-1} for *Np* and 1497–1509 cm^{-1} for *Ct*). The frequency of ν_3 is larger by ~10 cm^{-1} for 5c-NO compared to 6c-(His)-NO hemes[13,49] and this doublet agrees with a minor proportion of 5c-NO heme as observed in absorption spectra. The C–C stretching ν_{10} is also sensitive to the coordination (1625–1635 cm^{-1} for 6c-(His)-NO and >1640 cm^{-1} for 5c-NO).[14,49,50] Here, the values of 1634 for *Np* and 1625 cm^{-1} for *Ct* agree with the 6c-(His)-NO state, but again with a very minor 5c-NO population at 20 °C (<10%) inferred from the small peak at 1645 cm^{-1}.

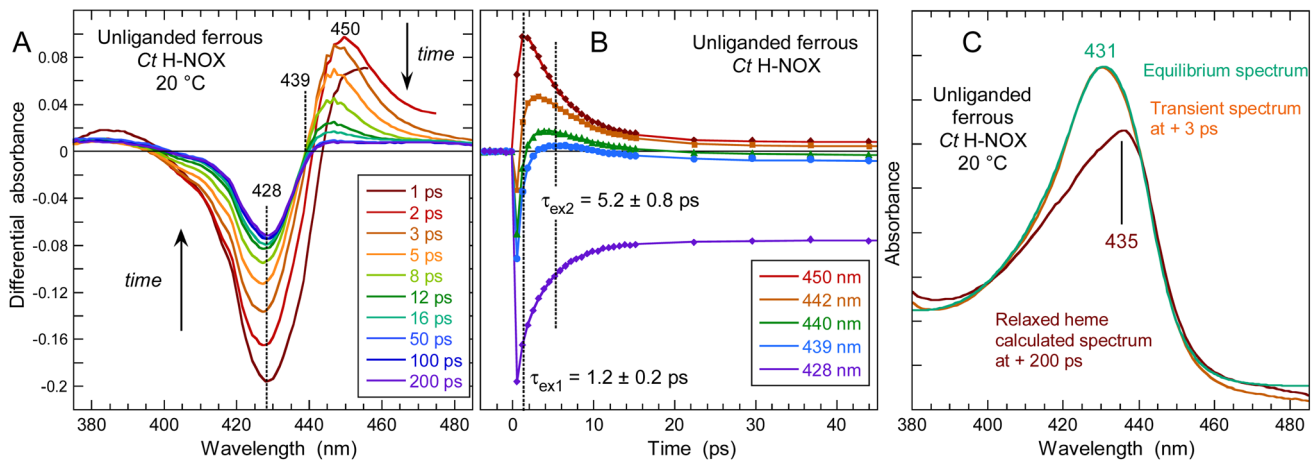

Fig. 6 (A) Transient spectra of the photo-excited 5c-His ferrous *Ct* H-NOX in the absence of NO. (B) Kinetics at particular wavelengths with fitted time constants of excited states decay. (C) Calculated spectrum of the relaxed heme 200 ps after photo-excitation (red) compared with the transient spectrum of the unliganded heme before excitation (−3 ps, orange) and steady-state spectrum of same sample (green). The sample was degased and placed in pure argon. The shift corresponds to $\Delta E = 214$ cm^{-1}.

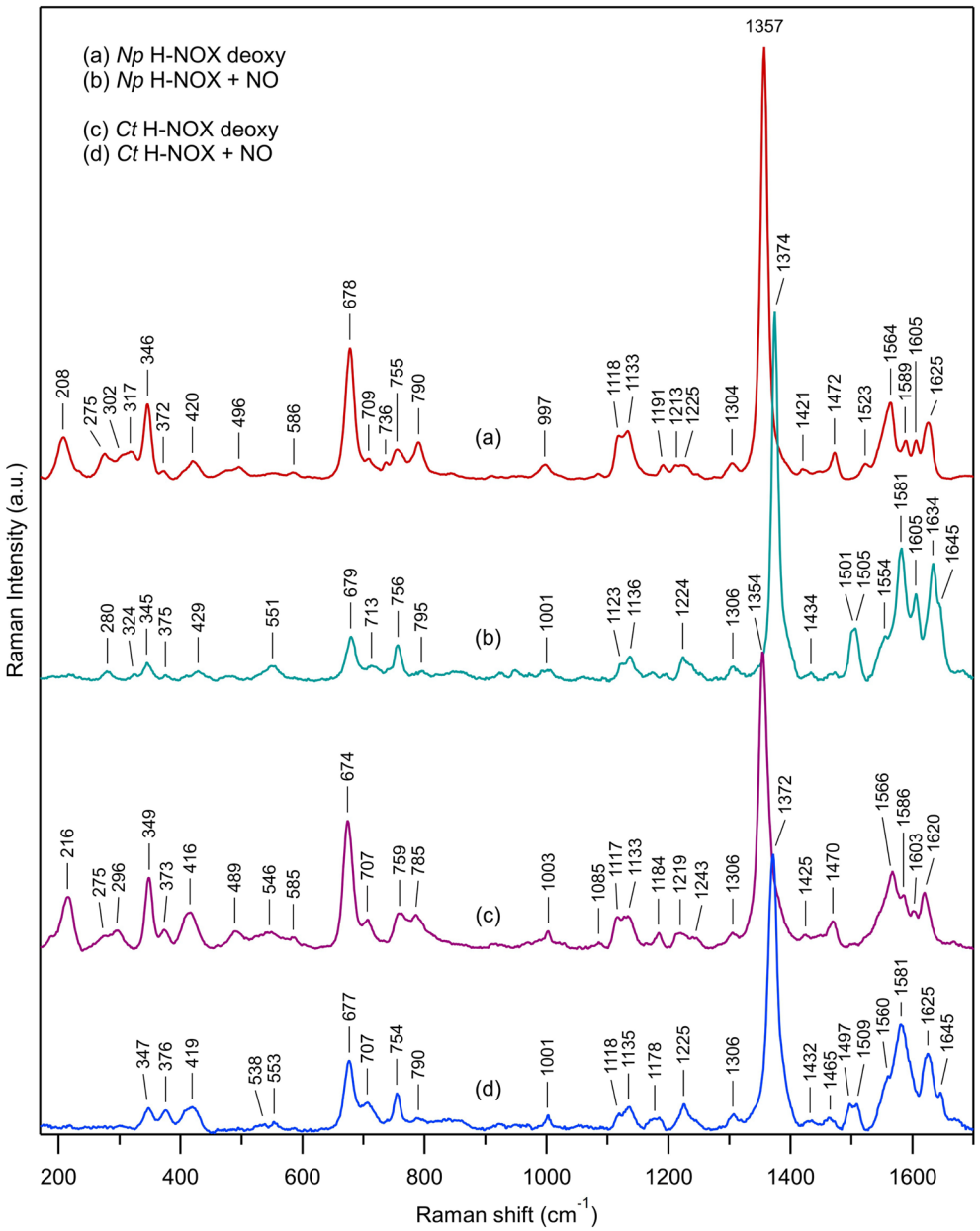

Fig. 7 Resonance Raman spectra of unliganded ferrous H-NOX and its corresponding nitrosylated analogs: (a) *Np* H-NOX deoxy; (b) *Np* H-NOX + NO; (c) *Ct* H-NOX deoxy; (d) *Ct* H-NOX + NO. Spectra were recorded with weak CW excitation at 442 nm. Raman bands assignment is given in ESI, Table S5.† $T = 20$ °C. [NO] = 200 μM. Enlarged view of the low frequency range in ESI, Fig. S15.†

Raman spectra of *Np* and *Ct* H-NOXs disclose differences linked with their markedly different responses after NO dissociation. Firstly, the ν(Fe–His) stretching frequency differs: 208 cm^{-1} for *Np*, close to that for sGC (204 cm^{-1}),[49,51,52] whereas the frequency for *Ct* (216 cm^{-1}) is closer to that of myoglobin (219 cm^{-1}).[53] A lower frequency translates a lower strength of the Fe^{2+}–His bond[54] which agrees with the easier formation of 5c-NO in *Np* at 20 °C compared with *Ct*.

Heme distortion can be probed by out-of-plane (*oop*) modes in the low frequency range (250–600 cm^{-1}).[55,56] Raman spectra appear conspicuously different in this range in the presence of NO (ESI, Fig. S15†). Especially, the *oop* γ_6 mode at 317 cm^{-1} in unbound *Np* (shifted to 324 cm^{-1} in the presence of NO) is also present in sGC[49] but not observed in *Ct*, either with or without NO. The *oop* mode γ_{21} (pyrrole folding),[53] whose intensity is sensitive to heme conformation and correlated with an increased heme ruffling[57,58] is present in *Ct* spectrum (546 cm^{-1}) but not observed in *Np* and sGC.[49,51] The *oop* mode ν_9 shifts from 275 to 280 cm^{-1} for *Np* after NO binding, but disappears for *Ct*. The intensity of the deformation mode $\delta(C_\beta–C–C)$ due to vinyl heme groups (420/416 cm^{-1}) decreased for *Np* but not *Ct*.

Overall, the low frequency range of the *Np* Raman spectrum is similar to that of sGC[49,51,52] showing that its heme adopts a conformation much closer to that of sGC than does *Ct* H-NOX

translating different heme–protein interactions[59] for *Ct*. The Raman spectra of *Np* and *Ct* appear different after NO binding, showing a differently altered heme conformation whereas *Np* and sGC[49] have similar Raman spectra in both unliganded and nitrosylated states.

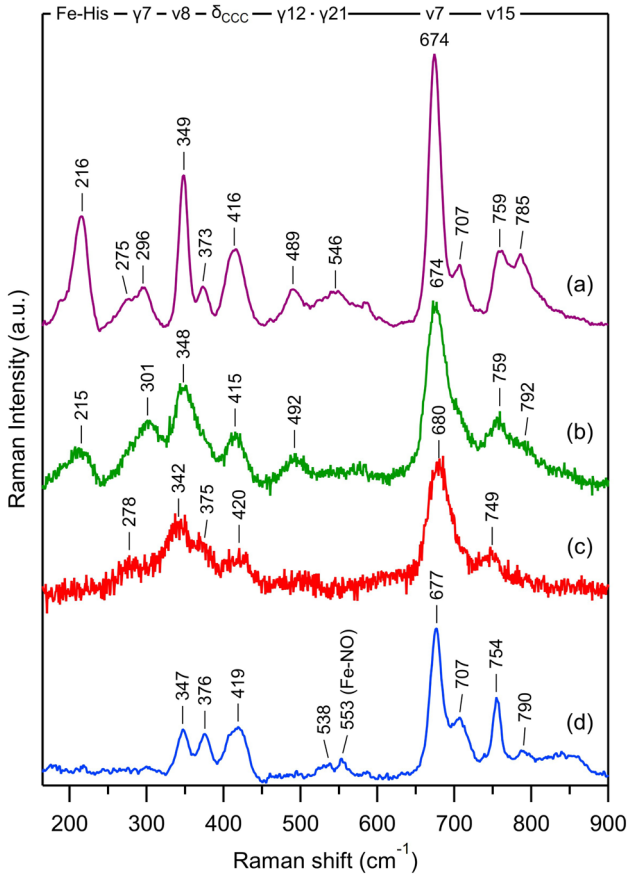

Fig. 8 Transient resonance Raman in low-frequency range compared to steady-state spectra of *Ct* H-NOX: (a) stationary *Ct* H-NOX deoxy species with CW excitation at 442 nm; (b) stationary *Ct* H-NOX deoxy species with sub-ps Raman excitation at 435 nm; (c) transient nitrosylated *Ct* H-NOX + NO with sub-ps pumping at 565 nm and probing at 435 nm, with time delay Δt = +2 ps between pump and probe pulses; (d) stationary nitrosylated *Ct* H-NOX with excitation at 442 nm. T = 20 °C.

Conformation of *Ct* H-NOX heme at +2 ps by time-resolved Raman spectroscopy

The very unusual reaction dynamics of *Ct* H-NOX after NO dissociation and its highly distorted heme in the 6c-(His)-NO state[15,60] led us to probe its conformation by time-resolved resonance Raman spectroscopy (TR^3).[61] The 0.7 ps Raman probe pulse (λ_{probe} = 435 nm) is necessarily spectrally broadened inducing a lower spectral resolution of the TR^3 spectrum compared to the steady-state one (Fig. 8a *versus* 8b and Table 2) but all modes could be resolved.

The transient Raman spectrum at Δt = +2 ps (Fig. 8c) represents the pure photoproduct after NO dissociation without contribution from non dissociated heme. The remarkable feature of this spectrum is the absence of the stretching mode ν(Fe–His) at Δt = +2 ps. This mode is a marker of the doming configuration of the 5c-His heme and located at 216 cm^{-1} for unliganded 5c-His *Ct* (Fig. 8a and b). Contrastingly, it was observed at Δt = +2 ps after NO dissociation for other proteins, including 6c-(His)-NO myoglobin and cytochrome *c*[38] and at Δt = +10 ps in 6c-(His)-CO sGC.[52] The transient absorption data of *Ct* H-NOX clearly indicate that a 5c-His heme is formed after photoexcitation (Fig. 5A), leading to discard the possibility that the TR^3 spectrum at Δt = +2 ps is due to electronic excited states. The absence of the mode ν(Fe–His) at Δt = +2 ps cannot be due to a photo-induced 4c heme from the 5c-NO species, like in cytochrome *c*′,[62] because *Ct* H-NOX is largely 6c-(His)-NO at 20 °C (>90%) as determined by the steady-state Raman and absorption spectra (Fig. 2C).

The absence of a transient ν(Fe–His) stretching mode after photodissociation of a diatomic ligand has been observed only for the bacterial O_2–sensor FixL[63] and explained by the ultrafast rebinding of dissociated O_2 which is maintained by a hydrogen bond with a side-chain of the heme pocket. This particular interaction results in Fe^{2+}–O_2 bond reformation in 4.7 ps (ref. 64) which was hypothesized to compete with heme doming, in contrast to myoglobin-NO.[38] We must emphasize that heme

Table 2 Assignments and frequencies (cm^{-1}) in TR^3 and CW spectra of *Ct* H-NOX in Fig. 8

Mode assignment	CW, NO-liganded	TR^3, photoproduct at + 2 ps	TR^3, unliganded (deoxy)	CW, unliganded (deoxy)
ν(Fe–His)	—	—	215	216
ν_9	—	~278 weak	Shoulder	275
γ_7 (pyr. *oop*)	—	—	301	296
ν_8	347	342	348	349
δ(C–C–C)	376	375	Shoulder	373
δ(C_β–C–C)	419	420	415	416
γ_{12}	—	—	492	489
γ_{21}	538 weak	—	—	546
ν(Fe–NO)	553	—	—	—
ν_7	677	680	674	674
γ_{11} (+γ_{15})	707	Shoulder	Shoulder	707
ν_{15}	754	749	759	759
ν_6	790	—	792	785

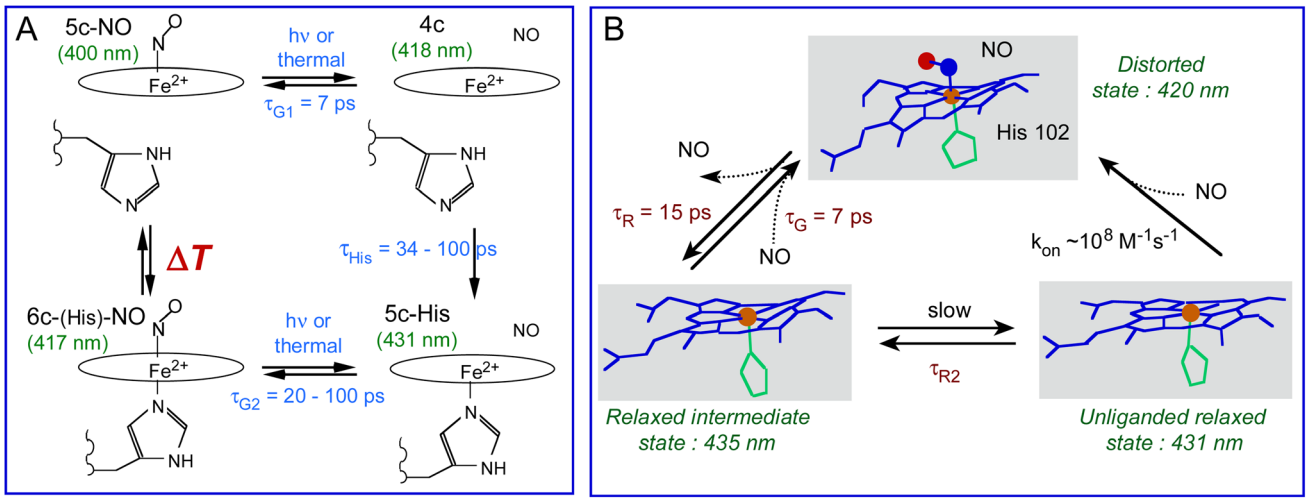

Fig. 9 (A) Coordination transitions of the heme in *Cb* and *Np* H-NOX sensors. The green values in parenthesis refer to the maximum of the Soret absorption band for *Np* H-NOX. The time constants are: τ_{His}, rebinding of the proximal His to Fe^{2+}; τ_{G1} and τ_{G2}, geminate rebinding of NO to Fe^{2+}. Importantly, the temperature range ΔT is different for *Cb* and *Np* species. (B) Allosteric equilibrium model incorporating heme distortion in the *Ct* H-NOX sensor and the time constants in Table 2. k_{on} is estimated to be diffusion limited ($\sim 10^8$ M^{-1} s^{-1}).[32]

doming only refers to Fe out-of-plane displacement whereas heme distortion involves the entire heme structure. In *Ct* H-NOX, NO geminately rebinds to the 5c-His heme with a 7 ps time constant as fast as it does to a 4c heme.[35,41,62] Furthermore, the transient absorption spectral evolution for *Ct*–NO H-NOX (Fig. 5) is completely different compared to FixL–NO,[64] notably disclosing a strong heme relaxation with a 15 ps time constant. NO geminate rebinding occurs before the relaxation of the heme which is still distorted at Δt = +2 ps, explaining the absence of the ν(Fe–His) stretching in TR^3 spectra. Indeed, the resonance conditions and intensity of the mode ν(Fe–His) depends on the overlap of Fe^{2+} and pyrroles electronic orbitals[65] which depends on the position of the Fe^{2+} atom with respect to the heme plane[38,65,66] but also on the heme distortion.[47,67–69] The importance of this effect is demonstrated by the decrease of heme redox potential in nitrophorin which favors the dismutase activity.[69] Fundamentally, we attribute the absence of the ν(Fe–His) band in the transient spectrum (+2 ps) to the high distortion which renders the 5c-His heme orbitals configuration less favorable for resonance, despite the out-of plane motion of Fe^{2+} due to NO dissociation.

Other features observed in the TR^3 spectra (Table 2) further indicates that the heme relaxation has not proceeded at Δt = +2 ps. The pattern located at 300–500 cm^{-1} is different between the TR^3 spectra of dissociated heme and stationary 5c-His heme. The mode ν_8 has a lower frequency (342 cm^{-1}, Fig. 8c) compared to the unliganded spectrum (348 cm^{-1}, Fig. 8b), whereas the mode γ_7 (301 cm^{-1}) is absent at Δt = +2 ps, indicating that the heme is not relaxed. The stretching mode ν_{15} is down shifted (749 cm^{-1}, Fig. 8c) with respect to its equilibrium value (759 cm^{-1}, Fig. 8b). The fast 7 ps NO recombination to the 5c-His heme of *Ct*, identical to that measured for 4c hemes,[35,62] strongly supports the view that the Fe^{2+} orbitals have a configuration as favorable as those of 4c heme. The constraints to an instantaneous iron doming should originate from the large saddling and ruffling *oop* distortions of the liganded heme,[57,60] contrarily to *Np* and *Cb* H-NOXs. Remarkably, O_2 rebinds to FixL and *Ct* H-NOX with similar time constants (4.7 and 5.1 ps respectively)[43,64] as NO does (5.3 and 7.1 ps), and a similar mechanism as described here may occur in FixL although its heme is less distorted as that of *Ct* H-NOX.

Theoretical DFT calculations[70] determined the absence of energy barrier for NO rebinding to a planar heme (heme–iron distance C_h–Fe = 0 Å) which corresponds to the fastest rate of NO geminate rebinding from within the heme pocket. For the larger iron displacement of a domed heme (C_h–Fe = 0.4 Å) the energy barrier is very small (3 kJ mol^{-1}).[70] We have experimentally measured the fastest rates in the range 5–7 ps with a slower component (23–38 ps) for 6c-(His)-NO (Table 1). Because for *Ct* H-NOX we did not observe slow components but only a fast one (7 ps) whatever the coordination state of the heme, 5c-NO or 6c-(His)-NO, we infer that the heme distortion[6] decreases (possibly to zero) the energy barrier of NO rebinding. Compared to *Np* and *Cb*, *Ct* H-NOX controls the NO affinity through a different mechanism which leads to a smaller k_{off} than that of *Cb* (Table S4†).

Implications and conclusion

In the bacterial sensors *Cb*, *Np* and *Ct* H-NOXs the proportion of 5c-NO heme increases as a function of temperature in contrast with mammalian sGC which is always 5c-NO, inducing more NO geminate rebinding to the 4c heme but the temperature range depends on the protein sequence. The H-NOX protein fold has thus the ability to modulate the activation energy for rupture of the Fe^{2+}–His bond triggered by NO binding and therefore can switch the mechanism of NO detection from 6c-(His)-NO to 5c-NO. The induced change of affinity is possible because k_{off} depends upon the heme proximal coordination,

being smaller for 5c-NO compared with 6c-(His)-NO heme by one or several orders of magnitude[32,71] due to the higher reactivity of the 4c heme to which NO rebinds in 7 ps with a high yield. This property driven by thermodynamics offers a mean of switching the sensor sensitivity for NO and adjusting the temperature range where it switches in order to adapt to living conditions of the bacteria. In human sGC it culminates with 100% population of 5c-NO heme whatever the temperature despite the same tertiary fold, but with the presence of a second NO binding site.[72] The molecular mechanism of bacterial H-NOXs depart from that of sGC, but the isolated heme domain of the latter discloses changed properties close to other H-NOXs.[34] Such adaptation for different reactivities of homologous proteins was also found in cytochromes from a methanotroph bacterium.[73]

In H-NOXs the information of NO binding is structurally conveyed through the motion of the proximal His. However, in *Ct* H-NOX the protein structure imposes heme distortion[6,7,60] and the structural relaxation of its distorted heme occurs rapidly after NO detachment (9–15 ps) at any temperature (Fig. 9B). This mechanism could be more adapted for a thermophilic organism with optimum growth at 75 °C, whatever the gas to be detected.

In conclusion, the modulation of the 6c-(His)-NO ↔ 5c-NO thermodynamic equilibrium has large consequences on the NO dynamics and NO affinity, connecting microscopic properties to macroscopic ones. The H-NOX structural fold has the ability to modulate the heme environment to provide organisms with precise properties through evolution, so that it became essential in various cell signaling pathways from bacteria to mammals.

Experimental methods

Detailed methods are provided in ESI.† Following is a brief report of the essential parameters.

Protein expression and preparation

The H-NOX bacterial sensors were overexpressed in *E. coli* as already described.[5] Isolated sGC was purified from beef lung (*Bos taurus*). For absorption measurements 90 μL of protein solution were placed in a quartz cell (1 mm optical path), degased then reduced under argon with sodium dithionite $Na_2S_2O_4$ (final concentration 0.5 mM). *Ct* H-NOX, purified in the O_2-liganded form, was briefly heated (70 °C) under Ar before reduction. NO-liganded H-NOX were obtained by introducing 10% NO (purity 99.999%) diluted in Ar directly into the cell (pressure 1.3 bar. [NO] = 200 μM in aqueous phase). Temperature was controlled by a thermostated cell holder. The absorbance of the nitrosylated H-NOXs was in the range 0.4–0.6 at the Soret maximum for 1 mm path length.

Time-resolved absorption spectroscopy

Transient absorption measurements were performed with the pump–probe laser system previously described.[74] The photodissociating (λ_{ex} = 564 nm) and probing pulses (broad band 375–550 nm) have a duration of ~50 fs with a repetition rate of 30 Hz and were spatially overlapped into the sample cell. The transient absorption spectra after a variable delay between pump and probe pulses were recorded with a CCD detector. Up to 50 scans were averaged. The data matrix of differential absorption as a function of time and wavelength was analyzed by singular value decomposition (SVD)[74] by using the software Glotaran.[75] Details of the SVD analysis are given in ESI Appendix 1.†

Resonance Raman spectroscopy

Resonance Raman spectra with continuous wave (CW) excitation were recorded with a He–Cd laser (441.6 nm) using the same Raman setup as for TR^3 studies. Time-resolved Raman apparatus has been described in detail elsewhere.[61] The excitation pulse (λ_{ex} = 560 nm) has a duration of 100 fs (repetition rate 1 kHz) and the probe pulse (λ_{pr} = 435 nm) has 0.7 ps temporal and 25 cm^{-1} spectral resolutions.

Ct H-NOX NO dynamic simulations

Molecular dynamic simulations based on classical mechanics were performed using CHARMM software[76] (version 36) over 250 ps with 1 fs integration steps. The model built from the PDB file 3tf0 comprises 39 595 atoms and was equilibrated at 273 K.

Data availability

The data supporting this article have been uploaded as part of ESI.†

Author contributions

S. G. K., C. S. R., P. N. and M. N. designed research. B. K. Y., S. G. K., J. C. L., I. L. and M. N. performed research. B. K. Y., S. G. K., J. C. L. and M. N. analyzed data. B. K. Y., S. G. K., P. N. and M. N. wrote the article.

Conflicts of interest

There are no conflicts to declare.

Acknowledgements

This work was supported by Institut National de la Santé et de la Recherche Médicale.

References

1 T. Shimizu, D. Huang, F. Yan, M. Stranava, M. Bartosova, V. Fojtíková and M. Martínková, *Chem. Rev.*, 2015, **115**, 6491–6533.
2 M. Negrerie, *Metallomics*, 2019, **11**, 868–893.
3 L. J. Ignarro, *Hypertension*, 1990, **16**, 477–483.
4 L. M. Iyer, V. Anantharaman and L. Aravind, *BMC Genomics*, 2003, **4**, 5.

5 P. Nioche, V. Berka, J. Vipond, N. Minton, A.-L. Tsai and C. Raman, *Science*, 2004, **306**, 1550–1553.
6 P. Pellicena, D. Karow, E. Boon, M. Marletta and J. Kuriyan, *Proc. Natl. Acad. Sci. U. S. A.*, 2004, **101**, 12854–12859.
7 M. A. Herzik, R. Jonnalagadda, J. Kuriyan and M. A. Marletta, *Proc. Natl. Acad. Sci. U. S. A.*, 2014, **111**, E4156—E4164.
8 E. M. Boon and M. A. Marletta, *J. Inorg. Biochem.*, 2005, **99**, 892–902.
9 J. M. Gray, D. S. Karow, H. Lu, A. J. Chang, J. S. Chang, R. E. Ellis, M. A. Marletta and C. I. Bargmann, *Nature*, 2004, **430**, 317–322.
10 S. H. Huang, D. C. Rio and M. A. Marletta, *Biochemistry*, 2007, **46**, 15115–15122.
11 B. G. Horst, E. M. Stewart, A. A. Nazarian and M. A. Marletta, *Biochemistry*, 2019, **58**, 2250–2259.
12 Y. Guo and M. A. Marletta, *ChemBioChem*, 2019, **20**, 7–19.
13 D. Karow, D. Pan, R. Tran, P. Pellicena, A. Presley, R. Mathies and M. A. Marletta, *Biochemistry*, 2004, **43**, 10203–10211.
14 E. M. Boon, J. H. Davis, R. Tran, D. S. Karow, S. H. Huang, D. Pan, M. M. Miazgowicz, R. A. Mathies and M. A. Marletta, *J. Biol. Chem.*, 2006, **281**, 21892–21902.
15 C. Olea, E. Boon, P. Pellicena, J. Kuriyan and M. A. Marletta, *ACS Chem. Biol.*, 2008, **3**, 703–710.
16 C. Olea, M. A. Herzik, J. Kuriyan and M. A. Marletta, *Protein Sci.*, 2010, **19**, 881–887.
17 X. Ma, N. Sayed, A. Beuve and F. van den Akker, *EMBO J.*, 2007, **26**, 578–588.
18 Y. Xue, Y. Xu, Y. Liu, Y. Ma and P. Zhou, *Int. J. Syst. Evol. Microbiol.*, 2001, **51**, 1335–1341.
19 M. L. Fardeau, M. Bonilla Salinas, S. L'Haridon, C. Jeanthon, F. Verhé, J.-L. Cayol, B. K. C. Patel, J.-L. Garcia and B. Ollivier, *Int. J. Syst. Evol. Microbiol.*, 2004, **54**, 467–474.
20 R. W. Castenholz and J. B. Waterbury, in *Bergey's Manual of Systematic Bacteriology*, 1989, vol. 3, pp. 1710–1728.
21 W. K. Erbil, M. S. Price, D. E. Wemmer and M. A. Marletta, *Proc. Natl. Acad. Sci. U. S. A.*, 2009, **106**, 19753–19760.
22 L.-M. Nisbett, L. Binnenkade, B. Bacon, S. Hossain, N. J. Kotloski, E. D. Brutinel, R. Hartmann, K. Drescher, D. P. Arora, S. Muralidharan, K. M. Thormann, J. A. Gralnick and E. M. Boon, *Biochemistry*, 2019, **58**, 4827–4841.
23 M. S. Price, L. Y. Chao and M. A. Marletta, *Biochemistry*, 2007, **46**, 13677–13683.
24 Y. Wang, Y. S. Dufour, H. K. Carlson, T. J. Donohue, M. A. Marletta and E. G. Ruby, *Proc. Natl. Acad. Sci. U. S. A.*, 2010, **107**, 8375–8380.
25 B. M. Henares, K. E. Higgins and E. M. Boon, *ACS Chem. Biol.*, 2012, **7**, 1331–1336.
26 T. Lahiri, B. Luan, D. P. Raleigh and E. M. Boon, *Biochemistry*, 2014, **53**, 2126–2135.
27 N. Liu, Y. Xu, S. Hossain, N. Huang, D. Coursolle, J. A. Gralnick and E. M. Boon, *Biochemistry*, 2012, **51**, 2087–2099.
28 V. Kumar, F. Martin, M. G. Hahn, M. Schaefer, J. Stamler, J.-P. Stasch and F. van den Akker, *Biochemistry*, 2013, **52**, 3601–3608.
29 Y. Kang, R. Liu, J.-X. Wu and L. Chen, *Nature*, 2019, **574**, 206–210.
30 A.-L. Tsai, V. Berka, F. Martin, X. Ma, F. van den Akker, M. Fabian and J. S. Olson, *Biochemistry*, 2010, **49**, 6587–6599.
31 B. K. Yoo, I. Lamarre, F. Rappaport, P. Nioche, C. S. Raman, J. L. Martin and M. Negrerie, *ACS Chem. Biol.*, 2012, **7**, 2046–2054.
32 G. Wu, W. Liu, V. Berka and A.-L. Tsai, *Biochemistry*, 2015, **54**, 7098–7109.
33 J. A. Winger, E. R. Derbyshire and M. A. Marletta, *J. Biol. Chem.*, 2007, **282**, 897–907.
34 B.-K. Yoo, I. Lamarre, J.-L. Martin and M. Negrerie, *J. Biol. Chem.*, 2012, **287**, 6851–6859.
35 M. Negrerie, L. Bouzhir, J. L. Martin and U. Liebl, *J. Biol. Chem.*, 2001, **276**, 46815–46821.
36 Y. Zhao, P. E. Brandish, D. P. Ballou and M. A. Marletta, *Proc. Natl. Acad. Sci. U. S. A.*, 1999, **96**, 14753–14758.
37 E. Martin, V. Berka, A.-L. Tsai and F. Murad, *Methods Enzymol.*, 2005, **396**, 478–492.
38 S. G. Kruglik, B.-K. Yoo, S. Franzen, M. H. Vos, J.-L. Martin and M. Negrerie, *Proc. Natl. Acad. Sci. U. S. A.*, 2010, **107**, 13678–13783.
39 M. L. Shelby, A. Wildman, D. Hayes, M. W. Mara, P. J. Lestrange, M. Cammarata, L. Balducci, M. Artamonov, H. T. Lemke, D. Zhu, T. Seideman, B. M. Hoffman, X. Li and L. X. Chen, *Proc. Natl. Acad. Sci. U. S. A.*, 2021, **118**, e2018966118.
40 B.-K. Yoo, I. Lamarre, J.-L. Martin, C. R. Andrew and M. Negrerie, *J. Am. Chem. Soc.*, 2013, **135**, 3248–3254.
41 B.-K. Yoo, I. Lamarre, J.-L. Martin, F. Rappaport and M. Negrerie, *Proc. Natl. Acad. Sci. U. S. A.*, 2015, **112**, E1697–E1704.
42 R. Liu, Y. Kang and L. Chen, *Nat. Commun.*, 2021, **12**, 5492.
43 O. N. Petrova, B.-K. Yoo, I. Lamarre, J. Selles, P. Nioche and M. Negrerie, *Commun. Chem.*, 2021, **4**, 31.
44 J. W. Petrich, C. Poyart and J.-L. Martin, *Biochemistry*, 1988, **27**, 4049–4060.
45 C. M. Drain, C. Kirmaier, C. J. Medforth, D. J. Nurco, K. M. Smith and D. Holten, *J. Phys. Chem.*, 1996, **100**, 11984–11993.
46 Y. Sun, A. Benabbas, W. Zeng, S. Muralidharan, E. M. Boon and P. M. Champion, *J. Phys. Chem. B*, 2016, **120**, 5351–5358.
47 A. B. Graves, M. T. Graves and M. D. Liptak, *J. Phys. Chem. B*, 2016, **120**, 3844–3853.
48 D. Kekilli, C. A. Petersen, D. A. Pixton, D. D. Ghafoor, G. H. Abdullah, F. S. N. Dworkowski, M. T. Wilson, D. J. Heyes, S. J. O. Hardman, L. M. Murphy, R. W. Strange, N. S. Scrutton, C. R. Andrew and M. A. Hough, *Chem. Sci.*, 2017, **8**, 1986–1994.
49 G. Deinum, J. R. Stone, G. T. Babcock and M. A. Marletta, *Biochemistry*, 1996, **35**, 1540–1547.
50 T. Tomita, T. Ogura, S. Tsuyama, Y. Imai and T. Kitigawa, *Biochemistry*, 1997, **36**, 10155–10160.
51 J. W. Denninger, J. P. M. Schelvis, P. E. Brandish, Y. Zhao, G. T. Babcock and M. A. Marletta, *Biochemistry*, 2000, **39**, 4191–4198.

52 J. P. M. Schelvis, Y. Zhao, M. A. Marletta and G. T. Babcock, *Biochemistry*, 1998, **37**, 16289–16297.
53 S. Hu, K. M. Smith and T. G. Spiro, *J. Am. Chem. Soc.*, 1996, **118**, 1638–12646.
54 T. Kitagawa, The heme protein structure and the iron-histidine stretching mode, in *Biological Applications of Raman Spectroscopy: Resonance Raman Spectra of Heme and Metalloproteins*, ed. T. G. Spiro, John Wiley & Sons, New York, 1988, vol. 3.
55 T. G. Spiro and X.-Y. Li, Resonance Raman spectroscopy of metalloporphyrins, in *Biological Applications of Raman Spectroscopy: Resonance Raman Spectra of Heme and Metalloproteins*, ed. T. G. Spiro, John Wiley & Sons, New York., 1988, vol. 3.
56 S. Choi and T. G. Spiro, *J. Am. Chem. Soc.*, 1983, **105**, 3683–3692.
57 Y. Sun, A. Benabbas, W. Zeng, J. G. Kleingardner, K. L. Bren and P. M. Champion, *Proc. Natl. Acad. Sci. U. S. A.*, 2014, **111**, 6570–6575.
58 S. G. Kruglik, B.-K. Yoo, J.-C. Lambry, J.-L. Martin and M. Negrerie, *Phys. Chem. Chem. Phys.*, 2017, **19**, 21317–21334.
59 F. Gruia, X. Ye, D. Ionascu, M. Kubo and P. M. Champion, *Biophys. J.*, 2007, **93**, 4404–4413.
60 C. W. Hespen, J. J. Bruegger, C. M. Phillips-Piro and M. A. Marletta, *ACS Chem. Biol.*, 2016, **11**, 2337–2346.
61 S. G. Kruglik, J.-C. Lambry, J.-L. Martin, M. H. Vos and M. Negrerie, *J. Raman Spectrosc.*, 2011, **42**, 265–275.
62 S. G. Kruglik, J. C. Lambry, S. Cianetti, J.-L. Martin, R. R. Eady, C. R. Andrew and M. Negrerie, *J. Biol. Chem.*, 2007, **282**, 5053–5062.
63 S. G. Kruglik, A. Jasaitis, K. Hola, T. Yamashita, U. Liebl, J.-L. Martin and M. H. Vos, *Proc. Natl. Acad. Sci. U. S. A.*, 2007, **104**, 7408–7413.
64 U. Liebl, L. Bouzhir-Sima, M. Negrerie, J.-L. Martin and M. H. Vos, *Proc. Natl. Acad. Sci. U. S. A.*, 2002, **99**, 12771–12776.
65 S. S. Stavrov, *Biophys. J.*, 1993, **6**, 1942–1950.
66 B.-K. Yoo, S. G. Kruglik, I. Lamarre, J.-L. Martin and M. Negrerie, *J. Phys. Chem. B*, 2012, **116**, 4106–4114.
67 J. A. Shelnutt, X.-Z. Song, J.-G. Ma, S.-L. Jia, W. Jentzen and C. J. Medforth, *Chem. Soc. Rev.*, 1998, **27**, 31–42.
68 J. G. Kleingardner and K. L. Bren, *Acc. Chem. Res.*, 2015, **48**, 1845–1852.
69 C. He, H. Ogata and W. Lubitz, *Chem. Sci.*, 2016, **7**, 5332–5340.
70 S. Franzen, *Proc. Natl. Acad. Sci. U. S. A.*, 2002, **99**, 16754–16759.
71 A.-L. Tsai, V. Berka, E. Martin and J. S. Olson, *Biochemistry*, 2012, **51**, 172–186.
72 G. Wu, I. Sharina and E. Martin, *Front. Mol. Biosci.*, 2022, **9**, 1007768.
73 H. R. Adams, C. Krewson, J. E. Vardanega, S. Fujii, T. Moreno, Chicano, Y. Sambongi, D. Svistunenko, J. Paps, C. R. Andrew and M. A. Hough, *Chem. Sci.*, 2019, **10**, 3031–3041.
74 M. Negrerie, S. Cianetti, M. H. Vos, J. L. Martin and S. G. Kruglik, *J. Phys. Chem. B*, 2006, **110**, 12766–12781.
75 J. J. Snellenburg, S. Laptenok, R. Seger, K. M. Mullen and I. H. M. van Stokkum, *J. Stat. Software*, 2012, **49**, 1–22.
76 B. R. Brooks, A. D. MacKerell, L. Nilsson, R. J. Petrella, B. Roux, Y. Won, G. Archontis, C. Bartels, S. Boresch, A. Caflisch, L. Caves, Q. Cui, A. R. Dinner, M. Feig, S. Fischer, J. Gao, M. Hodoscek, W. Im, K. Kuczera, T. Lazaridis, J. Ma, V. Ovchinnikov, E. Paci, R. W. Pastor, C. B. Post, J. Z. Pu, M. Schaefer, B. Tidor, R. M. Venable, H. L. Woodcock, X. Wu, W. Yang, D. M. York and M. Karplus, *J. Comput. Chem.*, 2009, **30**, 1545–1614.